LETTERS
PUBLISHED ONLINE: 26 OCTOBER 2015 | DOI: 10.1038/NCLIMATE2837

nature climate change

Accelerated dryland expansion under climate change

Jianping Huang*, Haipeng Yu, Xiaodan Guan, Guoyin Wang and Ruixia Guo

Drylands are home to more than 38% of the total global population and are one of the most sensitive areas to climate change and human activities[1,2]. Projecting the areal change in drylands is essential for taking early action to prevent the aggravation of global desertification[3,4]. However, dryland expansion has been underestimated in the Fifth Coupled Model Intercomparison Project (CMIP5) simulations[5] considering the past 58 years (1948–2005). Here, using historical data to bias-correct CMIP5 projections, we show an increase in dryland expansion rate resulting in the drylands covering half of the global land surface by the end of this century. Dryland area, projected under representative concentration pathways (RCPs) RCP8.5 and RCP4.5, will increase by 23% and 11%, respectively, relative to 1961–1990 baseline, equalling 56% and 50%, respectively, of total land surface. Such an expansion of drylands would lead to reduced carbon sequestration and enhanced regional warming[6,7], resulting in warming trends over the present drylands that are double those over humid regions. The increasing aridity, enhanced warming and rapidly growing human population will exacerbate the risk of land degradation and desertification in the near future in the drylands of developing countries, where 78% of dryland expansion and 50% of the population growth will occur under RCP8.5.

Drylands are defined as regions where precipitation is counterbalanced by evaporation from surfaces and transpiration by plants (evapotranspiration)[3]. Because most dryland soil is relatively infertile and the vegetation cover is sparse, dryland ecosystems are substantially more fragile[1]. Desertification and degradation are pervasive in drylands owing to global warming and the effects of rapid economic development, population growth and urbanization[8]. There are also some studies indicating that the increasing hydroclimatic intensity will become a predominant signature of twenty-first-century warming, which leads to shorter, less frequent, and less widespread precipitation events and an increase in the length of dry spells[9]. These trends may induce the expansion of drylands and further increase the fraction of the population that is affected by water scarcity and land degradation[1,4]. Knowledge of how climate change will affect the extent of drylands in the future is essential for their protection and for adaptation strategies[10]. The CMIP5 has generated projections using several emissions scenarios[11] and has provided a crucial reference for maintaining drylands as renewable resources. This study verifies CMIP5 simulations and bias-corrects the projections using historical observational data to provide a clear understanding of the spatial and temporal evolution of drylands in the future. The results may motivate decision makers to respond early and effectively to mitigate the pending global desertification.

The aridity of a region is generally measured by the aridity index (AI), which is the ratio of total annual precipitation to potential evapotranspiration (PET). Under this quantitative indicator, drylands are defined as regions with AI < 0.65 and are further divided into subtypes of hyper-arid (AI < 0.05), arid ($0.05 \leq$ AI < 0.2), semiarid ($0.2 \leq$ AI < 0.5) and dry subhumid ($0.5 \leq$ AI < 0.65) regions[3]. The observational data used here are from the Climate Prediction Center (CPC; refs 12,13). The simulation data are from 20 global climate models of CMIP5 (ref. 11; Methods). As the ensemble mean of these CMIP5 models (CMIP5-EM) can filter the uncertainty from inter-model variability and is the best representation of the response to imposed external forcing, it is better at predictions than any individual member[14,15] and is used to reflect the simulated aridity changes in this study.

To ensure the reliability of the future projections (2006–2100), it is critical to evaluate CMIP5-EM historical simulations (1948–2005) of dryland variability compared with observations over the same time period[5]. The historical values of the global observed AI and CMIP5-EM values over 58 years are compared in Table 1 and Fig. 1. The observed AI decreased remarkably, with a mean net trend of -0.050 per 58yr; the areas with drying trend cover up to 66% of the global land area (Table 1). By contrast, the mean trend of CMIP5-EM is only -0.012 per 58yr, which is approximately one-fourth of the observed trend; drying regions cover only 59% of the global land area. A subset of the AI data over the last 15 years of the historical period (1991–2005) is compared with the first 15 years (1948–1962) to highlight the temporal changes (Table 1). The observed areal increases in hyper-arid, arid, semiarid and subhumid land types from neighbouring wetter subtypes are 0.62%, 1.16%, 2.32% and 3.32%, respectively, of the global land area, whereas the increases according to CMIP5-EM are 0.05%, 0.14%, 0.37% and 0.50%, respectively. Similarly, the decreases in the subtype areas from drier to neighbouring wetter subtypes in CMIP5-EM are approximately one-third of those of the observations.

Because the observed changes are subject to both natural and forced variability, the above inconsistency could result from natural variability[16], the uncertainty of model configuration[17] and the uncertainty of external forcing in models[5]. Therefore, CMIP5-EM alone is not adequate for projecting future aridity changes, and corrections are necessary. By establishing a mapping relationship with historical observations, we conducted bias corrections[18–20] on CMIP5-EM (Methods). A posteriori independent validation indicated that the simulated aridity changes are more consistent with observations after correction (Supplementary Section 5). This result suggests that the relationship established from the historical period can also be applied in the future, and correcting the CMIP5-EM projections will be useful for evaluating global changes in aridity and aridity patterns.

Figure 2 presents the time series of the global mean AI and the areal changes in both the total drylands and the four subtypes of

Key Laboratory for Semi-Arid Climate Change of the Ministry of Education, College of Atmospheric Sciences, Lanzhou University, Lanzhou 730000, China.
*e-mail: hjp@lzu.edu.cn

Table 1 | Comparison of the AI for the observed data and CMIP5-EM simulation.

		Observed data	CMIP5-EM simulation
Percentage of global land area with drying trend during 1948–2005*		66%	59%
Linear trend of global mean AI during 1948–2005†		−0.050 per 58yr	−0.012 per 58yr
Neighbouring subtype changes during 1991–2005 relative to 1948–1962‡	Arid to hyper-arid	0.62	0.05
	Semiarid to arid	1.16	0.14
	Subhumid to semiarid	2.32	0.37
	Humid to subhumid	3.32	0.50
	Hyper-arid to arid	0.27	0.14
	Arid to semiarid	0.78	0.27
	Semiarid to subhumid	0.68	0.23
	Subhumid to humid	0.95	0.34

*See details in Fig. 1. †See details in Fig. 2. ‡Unit: percentage of global land area.

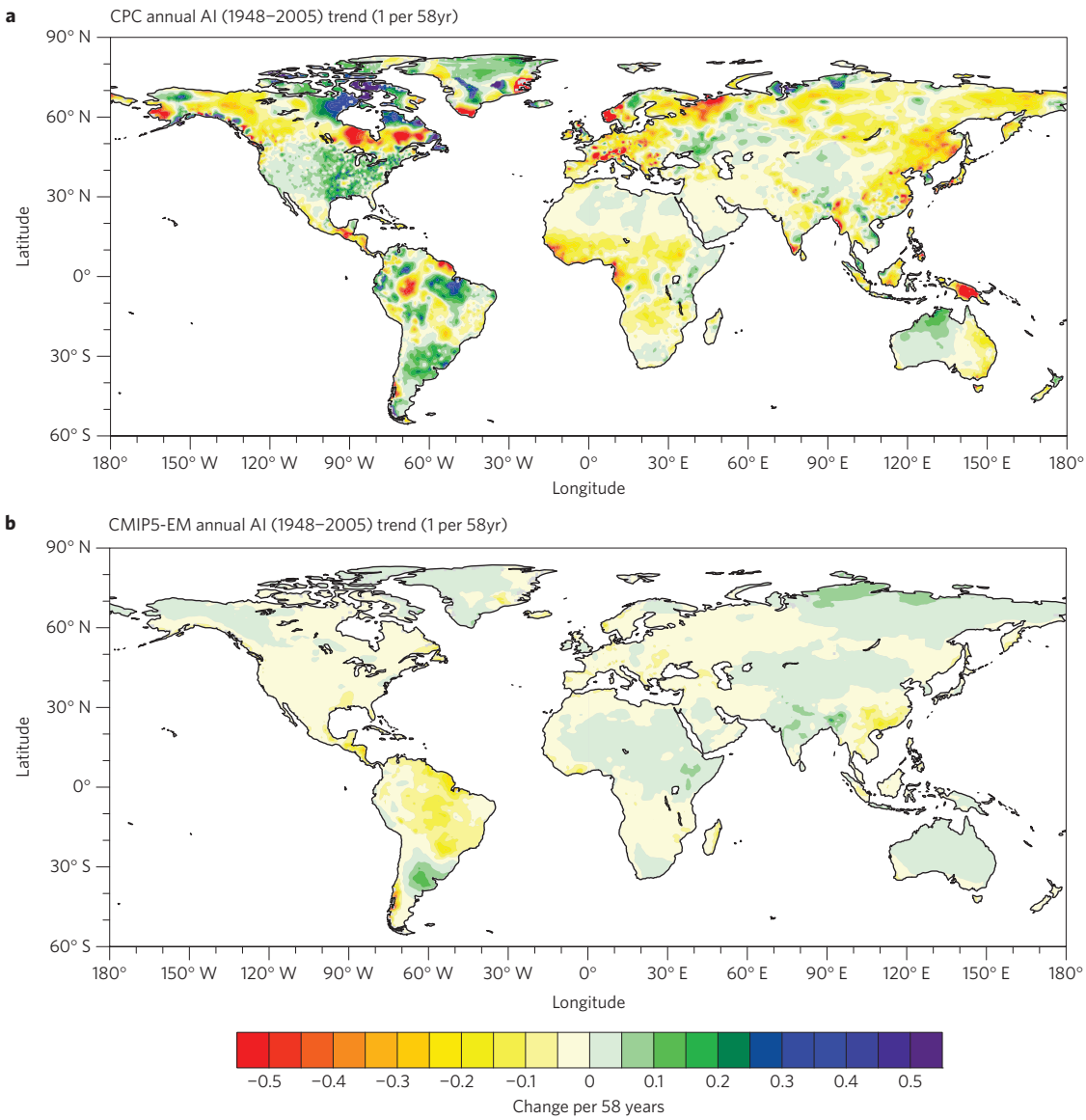

Figure 1 | Global distribution of the linear trend of AI for 1948–2005. a,**b**, The trend is based on the 58-year slopes from the CPC observations (**a**) and the CMIP5-EM historical simulations (**b**).

drylands for the historical and future periods. Clearly, the expansion of drylands in the historical period is severely underestimated by CMIP5-EM. The corrected CMIP5-EM reduced this underestimate and its spatial variations such that the simulation is comparable to the observations. For future projections, the corrected mean AI decreases monotonically and reaches values of 0.67 and 0.72 in 2100 under the Representative Concentration Pathway 8.5 (RCP8.5) and RCP4.5, respectively, whereas the original CMIP5-EM decreases

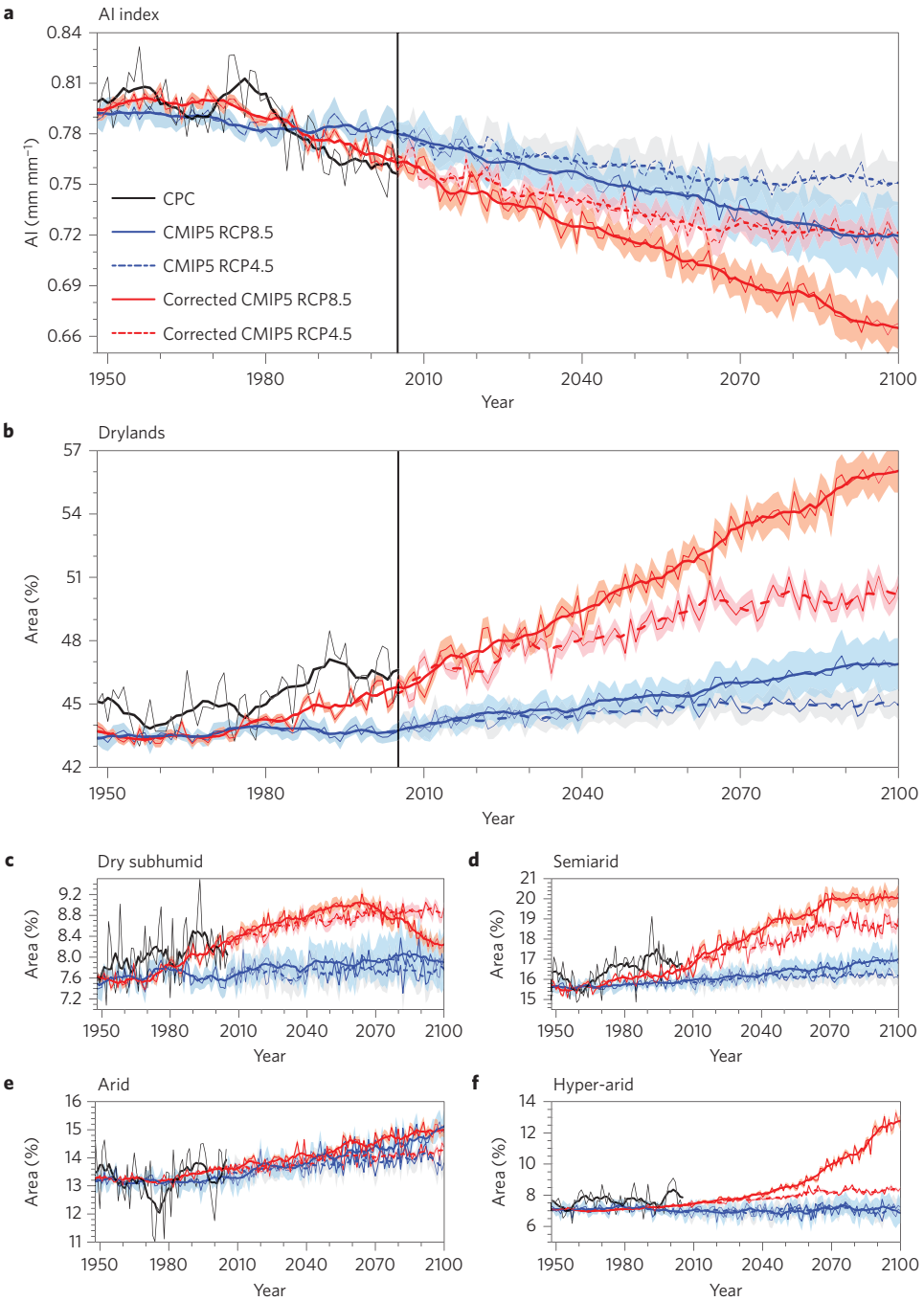

Figure 2 | Temporal variation in the global mean AI and the areal coverage of drylands. a–f, Global mean AI is shown in **a**, and areal coverage (percentage of global land area) is shown for total drylands (**b**), dry subhumid regions (**c**), semiarid regions (**d**), arid regions (**e**) and hyper-arid regions (**f**). The thin black lines are the CPC observations. The thin blue solid (dashed) lines are the CMIP5-EM from the historical and RCP8.5 (RCP4.5) projections. The thin red solid (dashed) lines are the corrected CMIP5-EM from the historical and RCP8.5 (RCP4.5) projections. The shading denotes the 95% confidence intervals of the 20 models. Seven-year running means (thick coloured lines) are shown to emphasize the aridity trends.

more slowly and reaches values of 0.72 and 0.75, respectively. According to the definition of drylands, the corrected area coverage is 56% of the global land area in 2100 under RCP8.5, which is 23% larger relative to observed climatology (1961–1990). The dryland subtypes of dry subhumid, semiarid, arid and hyper-arid comprise 8.3%, 20.3%, 14.9% and 12.6% of the global land area, respectively. Under RCP4.5, the total coverage is 50%, and the corresponding subtypes comprise 8.9%, 19.0%, 14.4% and 8.4% of the global land area. The largest expansion of drylands occurs in semiarid regions, which account for nearly half of the total dryland expansions in both RCP8.5 and RCP4.5 and cover more than one-third of the total drylands.

The future period is divided into three 30-year intervals to study the temporal evolution of the drylands. In the early twenty-first century (Fig. 3a), dryland expansion is not evident, and the distribution is scattered; additional semiarid and dry subhumid areas generally appear along the periphery of the original, historical drylands and increased arid and hyper-arid areas appear in Alaska, NW Canada and eastern Siberia. In the mid-twenty-first century (Fig. 3b), the subtype changes become more significant. The

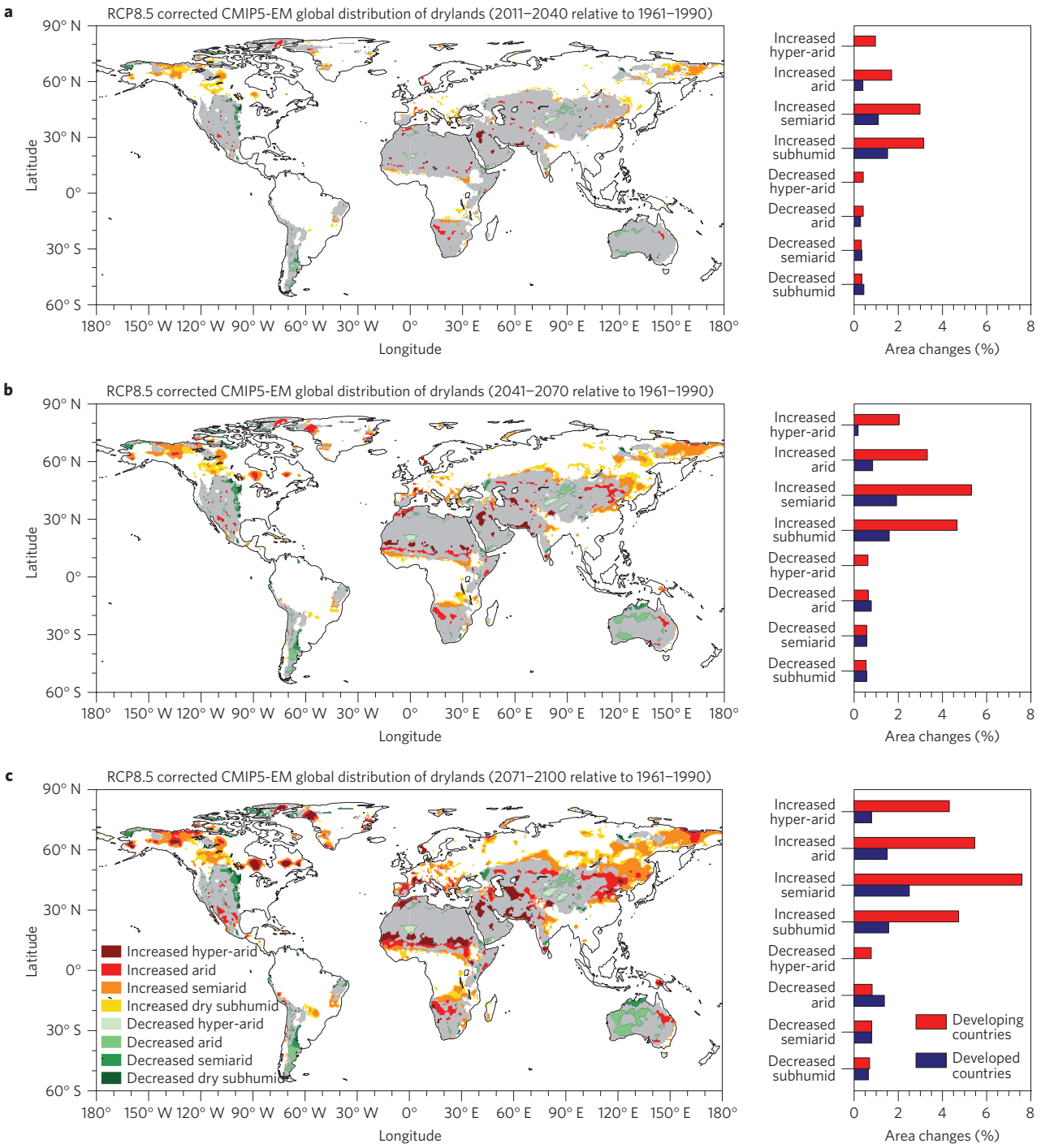

Figure 3 | Global distribution of future changes in the dryland subtypes. a–c, Projections of subtype changes from the corrected CMIP5-EM and RCP8.5 are shown relative to the baseline period (1961–1990) for 2011–2040 (**a**), 2041–2070 (**b**) and 2071–2100 (**c**) with the corresponding area changes (units: percentage of global land area) in developing and developed countries. The grey shading denotes the baseline drylands in 1961–1990. Changes include any transition from adjacent and nonadjacent subtypes. For example, the 'increased' category means the indicated regions transitioned from any of the subtypes, for example, semiarid, dry subhumid and humid to a drier subtype; the 'decreased' category refers to transitions from drier to wetter subtypes.

drying areas are mainly distributed in eastern Siberia, northeastern China, western Asia, central Africa and Canada, whereas the areas that become wetter mainly appear along the western half of the continents. Clearly, the subtypes that become drier comprise a much larger area than the subtypes that become wetter. In the late twenty-first century (Fig. 3c), the extent of the drier areas increases, and the drylands cover nearly all of the continental areas of Africa and Eurasia between 30° to 60° N and 15° to 50° S and western North America; thus, drylands dominate the global land surface. These results support previous studies[21,22] that the aridity changes over land have not simply followed the 'dry gets drier, wet gets wetter' paradigm. Figure 3 also indicates that 78% of the increased drylands occur in developing countries, but the area changes to wetter subtypes are much less, and the percentages in developing

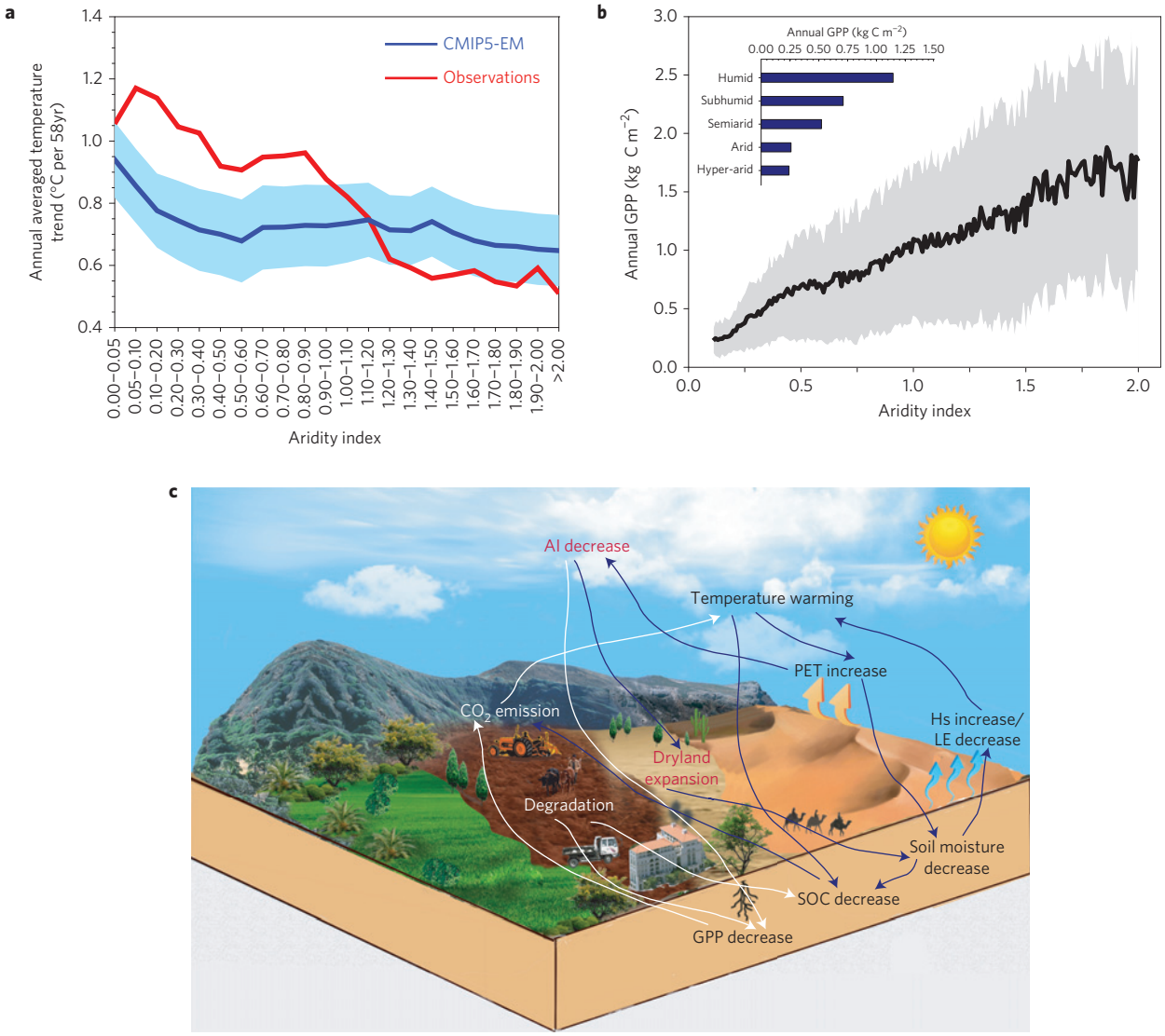

Figure 4 | Warming and drying feedback and associated impacts related to AI. a, Variation in the regionally averaged annual temperature trends (1948–2005), as calculated from CRU observations (red) and CMIP5-EM simulations (blue); the shading denotes the 95% confidence intervals. **b**, Annual GPP as a function of the AI; the black line denotes the regional mean from 2000 to 2010, with the grey shading denoting one standard deviation. The regional mean annual GPP of each subtype is shown in the inset. **c**, A schematic diagram of positive feedback cycles, including processes of global warming, dryland expansion and carbon emissions from soils.

countries and developed countries are equivalent. These results imply that the survival environment in developing countries will be more vulnerable.

Warming and drying trends occur in the historical period, and both are projected to persist into the future. Thus, these two factors may be linked through dynamics and climate. The warming may aggravate the dryland expansion by causing a higher vapour pressure deficit and evaporative demand, and the decreased soil moisture may lead to an increase in the sensible heat flux (Hs) and a decrease in the latent heat flux (LE; refs 23,24), and have an even stronger impact on temperature extremes[25,26]. Figure 4a shows that the average temperature increase is most significant in the drylands, with a warm peak of 1.17 °C per 58yr, which is approximately 2.1 and 1.5 times greater than the increase in humid regions and in the global mean, respectively. Furthermore, soil organic carbon (SOC) storage decreases with increasing temperature and increases with increasing soil water content[27]. Erosion-induced land degradation may also lead to the emission of carbon[28]. Therefore, against the background of global warming, the expansion of drylands will reduce the SOC storage and emit CO_2 into the atmosphere. Furthermore, the soil degradation and reduced soil moisture severely constrain the gross primary production (GPP; ref. 29) and affect the photosynthesis rate of plants that can absorb CO_2 and store carbon. As shown in Fig. 4b, the GPP is positively correlated with the AI, and the GPP in arid regions is approximately one-fifth of that in humid regions. By these two processes, dryland soils store less carbon and emit more CO_2 into the atmosphere, aggravating global warming. These processes result in a positive feedback cycle, with the warming and drying reinforcing each other (Fig. 4c). Unfortunately, CMIP5 cannot reproduce this pattern without large uncertainty (Fig. 4a) because global carbon cycle processes are not included in some CMIP5 models.

We can draw three main conclusions. First, drylands will expand by 23% and 11% relative to the observed baseline (1961–1990) by the end of the twenty-first century and will respectively cover a total of 56% and 50% of the global land surface under RCP8.5 and RCP4.5. Approximately 78% of the newly expanded dryland areas will be located in developing countries, where drylands will

comprise approximately 61% of these countries' total area by the end of the twenty-first century under RCP8.5. Compared with developed countries, the drylands in developing countries are more sensitive to climatic and environmental changes as well as to human-induced perturbations. Second, the warming trends over drylands, particularly in arid regions, are twice as great as those over humid regions. The same temperature rise will probably have a greater effect on the poor and vulnerable populations inhabiting the drylands, leading to increased poverty, degradation of the land and ecosystems, soil loss and further desertification[30]. Third, by 2025, drylands may occupy 48% of the global land surface and sustain 51% of the global population growth from 2000 to 2025, 50% of which will occur in developing countries, compared with only 1% in developed countries (Supplementary Fig. 10b). The population growth rate for any dryland subtype in developing countries is higher than that in humid regions (Supplementary Fig. 10c). Population growth will demand more agricultural production, such as tillage, pasturage and other human activities, which can quickly induce the degradation of sensitive drylands.

It should also be noted that, although the projection skill was improved by this correction method, the improvement is still limited because the correction method is based on the statistical mapping relationship between the observation and model output. The risk of dryland expansion proposed in our study still exists when results are based only on the projection of the original CMIP5; and this correction method suggests that the drylands will acceleratingly expand and the situation may be worse, especially in developing countries, a fact that is usually ignored by the public. Thus, developing countries will be exposed to three threats: extended drought, enhanced warming[6,7] and rapid population growth. These dire prospects and their interactions may accumulate in a nonlinear manner as a result of positive feedback in the climate aridity cycle; thus, the survival environment may become more vulnerable, and slight human disturbances can be disastrous. The risk of degradation and desertification will be far higher than the present expectations. As developing countries account for more than 70% of the global land area and population, degradation and desertification will become a challenge to the global ecosystem and human survival in the near future. Strict management and rational utilization of water resources, along with the restoration of soils and vegetation to reduce ecosystem vulnerability on a global scale, are urgently needed to develop a global action plan to prevent future desertification and eradicate the present global desertification problems.

Methods

Methods and any associated references are available in the online version of the paper.

Received 30 March 2015; accepted 22 September 2015; published online 26 October 2015

References

1. Reynolds, J. F. *et al.* Global desertification: Building a science for dryland development. *Science* **316,** 847–851 (2007).
2. GLP *Science Plan and Implementation Strategy* IGBP Report No. 53/IHDP Report No. 19 (IGBP Secretariat, 2005); http://www.globallandproject.org/arquivos/report_53.pdf
3. Middleton, N. & Thomas, D. *World Atlas of Desertification* (Oxford Univ. Press, 1997).
4. Reynolds, J. F. Scientific concepts for an integrated analysis of desertification. *Land Degrad. Dev.* **22,** 166–183 (2011).
5. Feng, S. & Fu, Q. Expansion of global drylands under a warming climate. *Atmos. Chem. Phys.* **13,** 10081–10094 (2013).
6. Huang, J., Guan, X. & Ji, F. Enhanced cold-season warming in semi-arid regions. *Atmos. Chem. Phys.* **12,** 5391–5398 (2012).
7. Ji, F., Wu, Z., Huang, J. & Chassignet, E. P. Evolution of land surface air temperature trend. *Nature Clim. Change* **4,** 462–466 (2014).
8. Fu, C. B. & Ma, Z. G. Global change and regional aridification. *Chin. J. Atmos. Sci.* **32,** 752–760 (2008).
9. Giorgi, F., Coppola, E. & Raffaele, F. A consistent picture of the hydroclimatic response to global warming from multiple indices: Models and observations. *J. Geophys. Res.* **119,** 11695–11708 (2014).
10. Nicholson, S. E. *Dryland Climatology* (Cambridge Univ. Press, 2011).
11. Taylor, K. E., Stouffer, R. J. & Meehl, G. A. An overview of CMIP5 and the experiment design. *Bull. Am. Meteorol. Soc.* **4,** 485–498 (2012).
12. Chen, M. Y., Xie, P. P., Janowiak, J. E. & Arkin, P. A. Global land precipitation: A 50-yr monthly analysis based on gauge observations. *J. Hydrometeorol.* **3,** 249–266 (2002).
13. Fan, Y. & Dool, H. V. D. A global monthly land surface air temperature analysis for 1948–present. *J. Geophys. Res.* **113,** D01103 (2008).
14. Reichler, T. & Kim, J. How well do coupled models simulate today's climate? *Bull. Am. Meteorol. Soc.* **89,** 303–311 (2008).
15. Pierce, D. W., Barnett, T. P., Santer, B. D. & Gleckler, P. J. Selecting global climate models for regional climate change studies. *Proc. Natl Acad. Sci. USA* **106,** 8441–8446 (2009).
16. Giorgi, F. & Bi, X. The Time of Emergence (TOE) of GHG-forced precipitation change hot-spots. *Geophys. Res. Lett.* **36,** L06709 (2009).
17. Giorgi, F. Climate change prediction. *Climatic Change* **73,** 239–265 (2005).
18. Ward, M. N. & Navarra, A. Pattern analysisof SST-forced variability in ensemble GCM simulations: Examples over Europe and the tropical Pacific. *J. Clim.* **10,** 2210–2220 (1997).
19. Feddersen, H., Navarra, A. & Ward, M. N. Reduction of model systematic error by statistical correction for dynamical seasonal predictions. *J. Clim.* **12,** 1974–1989 (1999).
20. Qin, Z. K., Lin, Z. H., Chen, H. & Sun, Z. B. The bias correction methods based on the EOF/SVD for short-term climate prediction and their applications. *Acta. Meteorol. Sin.* **69,** 289–296 (2011).
21. Greve, P. *et al.* Global assessment of trends in wetting and drying over land. *Nature Geosci.* **7,** 716–721 (2014).
22. Roderick, M. L., Sun, F., Lim, W. H. & Farquhar, G. D. A general framework for understanding the response of the water cycle to global warming over land and ocean. *Hydrol. Earth Syst. Sci.* **18,** 1575–1589 (2014).
23. Seneviratne, S. I. *et al.* Investigating soil moisture–climate interactions in a changing climate: A review. *Earth Sci. Rev.* **99,** 125–161 (2010).
24. Sherwood, S. & Fu, Q. A drier future? *Science* **343,** 737–739 (2014).
25. Seneviratne, S. I., Donat, M., Mueller, B. & Alexander, L. V. No pause in the increase of hot temperature extremes. *Nature Clim. Change* **4,** 161–163 (2014).
26. Hirschi, M. *et al.* Observational evidence for soil-moisture impact on hot extremes in southeastern Europe. *Nature Geosci.* **4,** 17–21 (2011).
27. Sharma, P., Abrol, V., Abrol, S. & Kumar, R. *Resource Management for Sustainable Agriculture*, Ch. 6 (InTech, 2012).
28. Lal, A. Carbon sequestration in dryland ecosystems. *Environ. Manage.* **33,** 528–544 (2003).
29. Peng, S. S. *et al.* Asymmetric effects of daytime and night-time warming on Northern Hemisphere vegetation. *Nature* **501,** 88–92 (2013).
30. Jiang, L. W. & Hardee, K. How do recent population trends matter to climate change? *Popul. Res. Policy Rev.* **30,** 287–312 (2011).

Acknowledgements

This work was jointly supported by the National Basic Research Program of China (2012CB955301), Special Public Welfare Research Fund of China (GYHY201206009), the National Science Foundation of China (41521004, 41305009 and 41405010) and the China University Research Talents Recruitment Program (111 project, No. B13045). The authors acknowledge the World Climate Research Programme's (WCRP) Working Group on Coupled Modelling (WGCM), the Global Organization for Earth System Science Portals (GO-ESSP) for producing the CMIP5 model simulations and making them available for analysis and NASA's Earth-Sun System Division (ESSD) for providing the MODIS Adaptive Processing System (MODAPS) data sets. All of the authors acknowledge S. Feng for providing the precipitation and PET data sets from the observations and the 20 members of CMIP5 and David Covert for his valuable comments and helpful suggestions for this research.

Author contributions

J.H. and H.Y. are first co-authors. J.H. designed the study and contributed to the ideas, interpretation and manuscript writing. H.Y. contributed to the data analysis, interpretation and manuscript writing. All authors contributed to the data analysis, discussion and interpretation of the manuscript. All authors reviewed the manuscript.

Additional information

Supplementary information is available in the online version of the paper. Reprints and permissions information is available online at www.nature.com/reprints. Correspondence and requests for materials should be addressed to J.H.

Competing financial interests

The authors declare no competing financial interests.

Methods

Observed data. (Details in Supplementary Sections 1 and 2).

The PRECipitation REConstruction over Land (PREC/L) data set developed by the CPC at a spatial resolution of 0.5° is involved in this study, which is interpolated from observations of the Global Historical Climatology Network (GHCN) version 2 and the Climate Anomaly Monitoring System (CAMS) data set for the period extending from 1948 to present[12]. The construction of the data set is introduced in Supplementary Section 1. In addition, the PET data set is provided by Feng and Fu[5], which is calculated using the Penman–Monteith method[31,32]. The surface air temperature (SAT) data set used to calculate PET is also from CPC, which is labelled as the GHCN_CAMS Gridded 2 m temperature[13]. The solar radiation, specific humidity and wind speed reanalysis data sets used are from the Global Land Data Assimilation System (GLDAS; ref. 33). The algorithms used for PET and the uncertainty and reliability of the Penman–Monteith method are discussed in Supplementary Section 2.

Simulated data. (Details in Supplementary Section 3).

The precipitation and PET simulation data set used are provided by Feng and Fu[5]. It is derived from monthly mean temperature, precipitation, solar radiation, specific humidity and wind speed products from 20 CMIP5 climate models[11] (Supplementary Table 2). Most of these simulations cover the period from 1850 to 2005 (ref. 11). Here, we analyse only the period from 1948 to 2005, for which the CMIP5, CPC and GLDAS data sets are commonly available. Because the CMIP5 models have different spatial resolutions, the simulated fields are statistically downscaled to a 0.5° × 0.5° resolution to match the observational data sets[5]. Moreover, to focus on the temporal variation and long-term climate change, the model simulations are adjusted to have the same climatology of 1961–1990 as the observations[5].

GPP data. The gross primary productivity (GPP) is the total amount of carbon fixed in the process of photosynthesis by plants in an ecosystem. A complete 11-year period (2000–2010) of yearly GPP data were acquired from NASA Goddard Space Flight Center (http://ladsweb.nascom.nasa.gov/data/search.html) to analyse the relationship between the AI and GPP. The yearly GPP data (MOD17A3) are retrieved at a spatial resolution of 1 km × 1 km as a part of the Terra satellite's Moderate Resolution Imaging Spectroradiometer (MODIS) level-4 collection 5.5 (C055), which was recently updated with yearly gridded land products. The data are processed by the MODIS Reprojection Tool (MRT) with a spatial grid cell resolution of 0.5° × 0.5°.

Population data. The population counts are from the Gridded Population of the World, version 3 (GPWv3) (http://sedac.ciesin.columbia.edu/gpw/index.jsp). A proportional allocation gridding algorithm, utilizing more than 300,000 national and sub-national administrative units, is used to assign population values for 2000 to grid cells with a spatial resolution of 0.5° × 0.5°. The population counts for 2025 are generated using the Country-level Population and Downscaled Projections Based on the Special Report on Emissions Scenarios (SRES) B2 Scenario (1990–2100) data set; CIESIN's Gridded Population of World, version 2 (GPWv2), is used as the base map[34].

Correction method. (Details in Supplementary Sections 4 and 5).

Because the CMIP5 and observed data over the historical period both have too many degrees of freedom, establishing a mapping relationship between them in such a high-dimensional space is impractical. By applying principal component analysis (PCA), the CMIP5 and observed data sets are both reduced to a lower dimensional space and decomposed into eigenvectors and corresponding principal components (PCs) (Supplementary Fig. 1). Each PC of the CPC data set is regressed by the leading PCs of CMIP5, and a matrix of regression coefficients is obtained. According to this relationship, the observed PCs can be predicted by the simulated PCs of CMIP5 in the future. The leading PCs are considered as correction factors not only because they are responsible for most of the variance in mathematics, but they also present high correlation with the patterns induced by external forces and by internal climate variability[35]. Although the correlation does not imply causality, it may reveal the possible physical meanings underlying each PC (see discussion in Supplementary Section 4.1). This method has been used to correct the seasonal predictions[18–20], and we adapted it in this study to correct the long-term changes of the CMIP5 projections.

The schematic of correction is shown in Supplementary Fig. 2 and the practical procedures are introduced as follows:

First, the simulated fields are corrected by subtracting the climate drift, which is estimated as the difference between the forecasts and the observations averaged over climatic timescales. Then the simulated field $Z_{\mathrm{sim}}(t)$ and observed field $Z_{\mathrm{obs}}(t)$ can both be expressed as a matrix of size $m \times n$, where m is the number of spatial grid points and n is the length of the time series. Generally, m is much larger than n. To reduce the spatial dimensions, we expand $Z_{\mathrm{sim}}(t)$ and $Z_{\mathrm{obs}}(t)$ by PCA:

$$Z_{\mathrm{sim}}(t) = \sum_{i=1}^{n} b_i(t) X_i \tag{1}$$

$$Z_{\mathrm{obs}}(t) = \sum_{j=1}^{n} a_j(t) Y_j \tag{2}$$

where X_i and Y_j are spatial patterns with a dimension of m; b_i and a_j are PCs corresponding to each X_i and Y_j with a dimension n. Using multiple linear regression, each $a_j(t)$ can be regressed by the K leading $b_i(t)$ $(i=1,2,\ldots,K)$:

$$a_j(t) = \sum_{i=1}^{K} b_i(t) c_{i,j} + e_j \tag{3}$$

where $c_{i,j}$ is the regression coefficient and e_j is the regression residual. Projecting $Z_{\mathrm{sim}}(n+1)$ (the predicted field at the time of $n+1$) onto each spatial pattern X_i will provide the corresponding time coefficient $b_i(n+1)$:

$$b_i(n+1) = X_i^{\,T}\, Z_{\mathrm{sim}}(n+1) \tag{4}$$

By inserting $b_i(n+1)$ into equation (3), we can obtain a prediction of the observed time coefficient

$$\widetilde{a}_j(n+1) = \sum_{i=1}^{K} b_i(n+1) c_{i,j} + e_j \tag{5}$$

Then, the adjusted prediction of Z_{obs} at a time of $n+1$ can be obtained by combining the spatial pattern:

$$\widetilde{Z}_{\mathrm{obs}}(n+1) = \sum_{j=1}^{K} \widetilde{a}_j(n+1) X_j \tag{6}$$

Generally, the climate models have a poor ability to simulate high-frequency variability, and retaining higher-order PCs may introduce additional noise. In this case, the optimal number of leading PCs should be examined. Here the widely used leave-one-out cross-validation during the historical period is conducted to choose the cumulative number of leading PCs (see detailed procedures in Supplementary Section 4.2 and Supplementary Fig. 3).

Because the corrected AI contains information from both observations and CMIP5, it is considered to be more accurate than the original projections. The validity of this method is verified by a posteriori independent validation (see details discussion in Supplementary Section 5), and the results confirm that the correction method is robust and reliable. On this basis, the PCA adjusting method is applied to the future period in the same way. The 58-year record of observations and simulations during the historical period is decomposed by PCA, and the linear regression is obtained. The simulation field for each year during the future period is projected onto the decomposed spatial patterns to obtain a time coefficient. Applying this time coefficient to the regression relationship will provide a 'predicted' time coefficient for the observations and allow a 'prediction' of the observed field. The adjustment is conducted for each year from 2006 to 2100 by obtaining the adjusted predictions under RCP8.5 and RCP4.5.

Graphics software. All maps and plots were produced using licensed IDL version 8.2.

References

31. Penman, H. L. Natural evaporation from open water, bare soil and grass. *Proc. R. Soc. Lond. A* **193,** 120–145 (1948).
32. Monteith, J. L. *Evaporation and Environment* 205–234 (Cambridge Univ. Press, 1965).
33. Rodell, M. The global land data assimilation system. *Bull. Am. Meteorol. Soc.* **85,** 381–394 (2004).
34. Gaffin, S. R., Rosenzweig, C., Xing, X. S. & Yetman, G. Downscaling and geo-spatial gridding of socio-economic projections from the IPCC special report on emissions scenarios (SRES). *Glob. Environ. Change* **14,** 105–123 (2004).
35. Dai, A. G. Increasing drought under global warming in observations and models. *Nature Clim. Change* **3,** 52–58 (2013).